Numerical simulation of the shear stress produced by the hot metal jet on the blast furnace runner

P. Barral [a,b], B. Nicolás [c], P. Quintela [a,b,*]

[a] *Departamento de Matemática Aplicada and Instituto de Matemáticas (IMAT), Universidade de Santiago de Compostela, 15782 Santiago de Compostela, Spain*
[b] *Technological Institute for Industrial Mathematics (ITMATI), Rúa Constantino Candeira s/n, 15782 Santiago de Compostela, Spain*
[c] *Departament Matemàtiques i Informàtica, Universitat de Barcelona, Gran Via de les Corts Catalanes 585, 08007 Barcelona, Spain*

ARTICLE INFO

ABSTRACT

During steel casting process a jet of molten metal runs out of the blast furnace hearth and strikes the runner. The continuous impact of hot fluids causes significant damage to its surface, which is made of refractory concrete. In particular, the initial impact on the dry runner is expected to be critical. This work deals with the analysis of the mechanical impact on the runner through the numerical simulation of the process. We propose an incompressible turbulent isothermal Navier-Stokes model, where turbulence is modelled considering two $k-\omega$ models (standard and SST). The interface dynamics is described by applying the Volume of Fluid (VOF) method, while the surface tension vector is provided by the Continuum Surface model (CSF). Their numerical results are performed in 2D. A comparative analysis of the most suitable transient turbulent multiphase model is presented by simulating benchmark physical experiments. The shear stress arising from the impact of the jet on the runner is also analyzed. An improvement of the classical analytical expression given in [1] is proposed. Both, the chosen turbulence model, and the formulas to compute the shear stress are validated using two benchmark laboratory tests and three numerical experiments. Numerical results are given for the impact of the jet on the dry runner of the blast furnace.

1. Introduction

A blast furnace is a furnace used for smelting ores to produce industrial metals. This paper focuses on blast furnaces operating by a steelmaking company, similar to that considered in [2], where the smelted ores, iron and carbon (coke), are used to generate pig iron, also known as hot metal, which is the raw material of steel.

At the top of the blast furnace there is the throat, see Fig. 1, through which the ores and fluxes are introduced. Hot air enriched with oxygen is injected under great pressure through the tuyeres, placed in the bosh. This air allows to hold the loads while the smelting process is performed. When the carbon ore contacts the air, several exothermic chemical reactions take place increasing the temperature inside the furnace, that can reach up to 1500 °C.

When the iron ore is smelted, the bottom of the blast furnace, called hearth, is drilled and metal fluids run out through the taphole. Its inclination is around 10 degrees upwards (see Fig. 1). So the hot fluids run out of the blast furnace like a jet describing a parabolic path until reaching the runner, also known as trough (see Fig. 2). After approx-

imately 60 minutes of casting, when the furnace gas starts going out, the taphole is plugged with clay. During the stop, the metal level in the furnace rises again. Once the necessary level is reached, a new casting cycle starts. In this way, the level of fluids in the hearth is kept as constant as possible for process safety [3]. So, the pressure inside the hearth and the velocity of fluids when running out through the taphole can be considered to be constant.

Inside the furnace, in addition to the hot metal, there is slag, formed by fluxes, gangues of minerals and ashes of coke. The density of the hot metal is much greater than that of the slag, therefore the metal is located in the lower part of the furnace and is the first to go out when the taphole is open. Afterwards, a mixture of metal and slag bubbles goes out. Since the diameter of the taphole is very small, we can assume that it is a mixture. Later, they will be separated again on the casting runner because of their different densities. It should be noted that the runner is slightly inclined to encourage fluids to move towards the end of the runner.

At the end of the runner, the slag at the top is deflected through the slag runner, while the hot metal goes down underneath the skimmer

---

* Corresponding author at: Departamento de Matemática Aplicada and Instituto de Matemáticas (IMAT), Universidade de Santiago de Compostela, 15782 Santiago de Compostela, Spain.
E-mail address: peregrina.quintela@usc.es (P. Quintela).

Table 1

Nomenclature.

| Magnitude	Description	Magnitude	Description
a_1	Adjustment coefficient for SST turbulence model	α, α^*	Adjustment coefficients for SST turbulence model
$\mathbf{b}_p$ (m/s^2)	Body force per unit of mass acting on phase p	α_p	Volume fraction of p-phase
$\mathbf{b}$ (m/s^2)	Effective body force per unit of mass	β, β^*	Adjustment functions for SST turbulence model
C_l	Cell	δ (adim)	Dirac delta function
d (m)	Taphole diameter	Δt (s)	Time step
d_n (mm)	Nozzle diameter	Γ	Solid-fluid interface
$\mathbf{D}(\mathbf{v})$ (1/s)	Symmetrical part of the velocity $\mathbf{v}$ gradient	Γ_{axis}	Boundary corresponding to the axis of the jet
D_ω (kg/(m^3 s^2))	Cross-diffusion term of ω	$\Gamma_{\text{in}}, \Gamma_{\text{out}}, \Gamma_{\text{wall}}$	Inlet, outlet and wall boundaries
F_1, F_2	Blending functions for SST turbulence model	Γ_k (kg/(ms))	Effective diffusivity term of k
Fr (adim)	Froude number	Γ_ω (kg/(ms))	Effective diffusivity term of ω
$\mathbf{g}, g$ (m/s^2)	Gravitational acceleration vector and modulus	κ (1/m^2)	Interface curvature between two phases
G_k (kg/(ms^3))	Generation term of k	λ (adim)	Relation between r and H
G_ω (kg/(m^3 s^2))	Generation term of ω	μ_{eff} (Pa s)	Effective fluid dynamic viscosity
H (mm)	Height from the nozzle to the wall	μ_f (Pa s)	Generical fluid dynamic viscosity
$\mathbf{I}$ (adim)	Identity matrix	μ_h (Pa s)	Hot metal dynamic viscosity
k (m^2/s^2)	Turbulence kinetic energy	μ_T (Pa s)	Turbulent fluid dynamic viscosity
k_{inlet} (m^2/s^2)	Inlet turbulence kinetic energy	$\mu_{T\,inlet}$ (Pa s)	Inlet turbulent fluid dynamic viscosity
k_d (m^2 s/kg)	Erosion kinetics coefficient per unit of mass	π, Π, Π^* (Pa)	Flow pressure, mean pressure and reduced pressure
k_{er} (s/m)	Erosion kinetics coefficient	ρ (kg/m^3)	Effective mass density
L_w (mm)	Size of the wall segment in normal jets simulation	ρ_f (kg/m^3)	Generical fluid mass density
$\dot{m}$ (kg/(m^2 s))	Eroded mass flux	ρ_h (kg/m^3)	Hot metal mass density
$\mathbf{m}^\sigma$ (kg/(m^2 s^2))	Surface tension vector	ρ_p (kg/m^3)	p-Phase mass density
M (adim)	Mach number	ρ_s (kg/m^3)	Generical solid porous media mass density
$\mathbf{M}_p$ (N/m^3)	Force of phase p due to interaction with other phases	σ (N/m)	Surface tension coefficient between two phases
$\hat{\mathbf{n}}$ (adim)	Unit vector normal to the interface between two phases	$\sigma_{h,a}$ (N/m)	Surface tension coefficient between hot metal and air
N_c	Cells number	σ_k, σ_ω	Prandtl numbers for k and ω
N_p	Number of immiscible phases	$\sigma_{\omega,2}$	Adjustment coefficient for SST turbulence model
r (mm)	Radial coordinate for normal jets simulations	τ (Pa)	Shear stress
Re (adim)	Reynolds number	τ_c (Pa)	Critical shear stress
S (1/s)	Strain rate magnitude	τ_{max}, τ_{min} (Pa)	Maximum and minimum shear stress
t (s)	Time	τ^R (Pa)	Reynolds stress tensor
$\mathbf{T}_p$ (Pa)	Stress tensor for phase p	ω (1/s)	Specific turbulence dissipation rate
$\mathbf{T}$ (Pa)	Effective stress tensor	ω_{inlet} (1/s)	Inlet turbulence dissipation rate
v_0 (m/s)	Exit velocity from the nozzle	Ω	Computational domain for jet impact simulation
v_{sound} (m/s)	Speed of sound	Ω_e	Computational domain for experiments simulation
v_Γ (m/s)	Solid-fluid interface modification velocity	Ω_{stag}	Stagnation zone
$\mathbf{v}, \mathbf{V}, \mathbf{v}'$ (m/s)	Flow velocity, mean velocity and velocity fluctuation		
$\mathbf{v}_p$ (m/s)	Velocity of phase p		
$\mathbf{v}'_{inlet}$ (m/s)	Hot metal velocity inlet fluctuation		
$\mathbf{V}_{inlet}, v_{inlet}$ (m/s)	Hot metal velocity inlet, vector and modulus		
We (adim)	Weber number		
x (m)	Horizontal coordinate for hot metal simulation		
y (m)	Vertical coordinate for hot metal simulation		
Y_k (kg/(ms^3))	Dissipation term of k		
Y_ω (kg/(m^3 s^2))	Dissipation term of ω		
z (m)	Vertical coordinate for normal jets simulations		
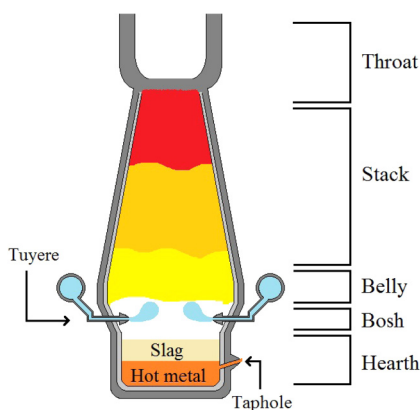
Fig. 1. Schematic view of a blast furnace.

and reaches the hot metal runner (see Fig. 2). Notice that after the skimmer there is a small vertical wall, so that hot metal level in this zone has to be high enough to go beyond it and to access to the hot metal runner. When a casting cycle finishes, the level of accumulated fluid is not enough for this to happen and a layer of fluid remains over the runner between two casting cycles. So, this hot fluid layer makes impossible to access the runner bottom surface until its useful life ends and, therefore, it is not feasible to take wear measurements while it is operating. For this reason, the numerical simulation of the jet impact is an essential tool.

Useful life of a casting runner is limited by several wear phenomena that take place during casting process. Wear is mainly due to chemical, thermal and mechanical phenomena. Chemical wear is due to the composition of the slag, which contains highly corrosive substances. On the other hand, extremely high temperatures are reached during casting process and they can cause the appearance of fluid phases inside the runner refractory concrete. Furthermore, when the hot metal jet first hits the runner, a thermal shock could be produced, although in practice this is mitigated by the use of heaters for raising the temperature of the refractory concrete. Finally, mechanical wear has its origin in the impact produced on the runner by the molten metal jet when running out of the blast furnace under pressure. Our interest is focused on the latter phenomenon, the mechanical wear. A more detailed description of the entire casting process can be found in [3].

Although there is abundant literature on numerical simulation of furnace behaviour (see for example [4–7]), there are not many papers on numerical simulation of the runner. So, the authors have devoted considerable effort to understanding its thermomechanical behaviour: first performing a stationary two-dimensional thermal analysis in the middle section of the runner in [8]; then, a three-dimensional ther-
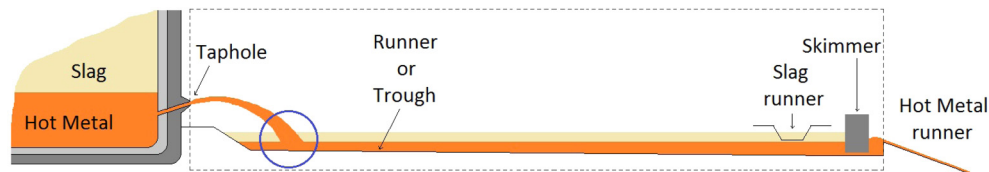
Fig. 2. Schematic longitudinal view of the runner. Impact zone is surrounded and computational domain is marked with dash-line.

mohydrodynamic model was solved to find the position of critical isotherms within solid refractory layers in [2]. In the latter and in the proceedings [9], a first numerical simulation of the impact of the hot metal jet falling from the blast furnace on the runner was presented. A simpler turbulence model, the Wilcox k-ω model, was used there [10]. A first objective of this work is to improve the jet hydrodynamic simulation. Since it is not possible to obtain experimental measures in blast furnace jets to validate numerical results, in this paper the authors present a comparative analysis of the Wilcox k-ω method with the Shear Stress Transport (SST) k-ω turbulence model on two benchmark laboratory tests registered in [1]. The analysis shows that the SST k-ω turbulence model is better at simulating shear stress produced by a jet on a wall.

In the previous papers [2,9] two scenarios were compared: the jet impact on dry trough versus on a narrow pool of hot metal. Numerical simulations shown that the maximum shear stresses produced by mechanical effects was obtained at the impact instant in the first scenario. Therefore the second objective of this work is to accurately compute the mechanical impact of the jet on the dry runner. More precisely, our interest is focused on the calculation of the exerted shear stress since its magnitude is considered in the bibliography the essential agent in the mechanical erosion, as can be seen in several references, from the earliest works by [11] to recent ones like the PhD thesis of [12] and her subsequent paper [13]. So, it is interesting to find an analytical formula to approximate them. In this sense, it is remarkable [1] work. They proposed a normalized shear stress equation adjustment from the experimental study of submerged air jets impinging normally over a rigid wall. Their equation has been widely applied, however, it presents some discrepancies with the laboratory experimental data as we move away from the impact point of centerline of the jet. In this paper we also propose a new adjustment equation to overcome these discrepancies. The proposed new formula is validated not only with the laboratory data from the benchmark cases mentioned above, but also with three additional numerical experiments. Numerical results with this method are presented and, in addition, a dynamic adaptive meshing is carried out that allows to improve the tracking of the jet and the calculation times.

Section 2 is devoted to the description of the jet impact problem. In order to carry out an accurate study of the impact, some preliminary analysis of the bibliography about erosion and turbulence models are performed in Section 3. Subsection 3.1 consists of an analysis of the mechanical erosion mechanisms, which allows to identify shear stress as the main magnitude to focus on. In Subsection 3.2, three benchmark laboratory tests are introduced and the classical formula of [1] is analyzed. Subsection 3.3 is devoted to propose an improvement of the later. In Subsection 3.4, a discussion of the most suitable turbulence model for this problem is included. Section 3 is completed with the validation of the proposed formula for the calculation of the shear stress on three numerical tests.

In Section 4, we come back to the jet impact problem arising in the casting process taking into account the conclusions drawn from the analysis of the previous section. Details about the involved models related to incompressible fluids, turbulence, and immiscible and multiphase fluids behaviour are given in its first subsections. The complete mathematical model associated to the jet impact problem is presented in Subsection 4.4. It corresponds to an incompressible turbulent multiphase flow in transient regime. Its numerical results can be found in Section 5. In particular, results are included on the shear stress with respect to the jet exit distance in the first moments of impact as well as the maximum pressure points.

Finally, some conclusions about the main results of this paper are presented in Section 6.

2. Jet impact problem

In this section we introduce the jet impact problem for its subsequent modelling and numerical simulation. Here, the explanation about how fluids run out of the blast furnace is presented, as well as their characterization in basis of the dimensionless numbers theory. To facilitate the reading of this document, a list of the notation used is included in Table 1.

For this study, computational domain corresponding to dash-line marked box in Fig. 2 is considered, focusing our attention on impact zone, surrounded by a circle in the same figure.

In this paper we focus on the first few seconds of a new casting, since afterwards, as it was proved in [9] the liquid pool on the runner cushions the impact of the jet. Notice that during this time interval just hot metal runs out the blast furnace, so two phases are involved: hot metal and air. Since hot metal density is almost three times slag density, let us remark that in this way, we are considering the worst case from the impact point of view.

As it was announced in the previous section, it is extremely difficult to measure the velocity at which the fluids run out the furnace, therefore it is assumed to be constant. To compute its value we have considered the following data:

- Hot metal and slag production amount at each casting cycle: $450E03$ kg and $100E03$ kg, respectively.
- Taphole diameter: $d = 0.06$ m.
- Material properties:

  $$\rho_h = 7015 \text{ kg/m}^3, \quad \mu_h = 7.15E - 03 \text{ Pa s},$$

  where ρ_h and μ_h are the hot metal density and its dynamic viscosity, respectively.
- Casting cycle duration: 5400 s.

All this information leads to the run out velocity modulus $v_{inlet} = 6.29$ m/s, named as velocity inlet, since this is the velocity at which hot metal enters the computational domain, shown in Fig. 2. Its value is considered constant and estimated using the mass flow computed from the previous data during the casting cycle, assuming that only hot metal comes out for the first 20 minutes and then a mixture of hot metal and slag comes out (see [14]). Dimensionless numbers study must be made in order to characterize the hot metal jet behaviour. Since we only know the data relative to hot metal in the taphole zone, the characterization is realized at the beginning of the fluid trajectory. Therefore, the characteristic velocity and length of the fluid considered are v_{inlet} and the taphole diameter, d, respectively. More details about dimensionless numbers characterising fluids can be found, for example, in [15].

- Mach number, M, is the relation between the fluid characteristic velocity and the speed of sound, v_{sound}. Therefore, considering the air near the hot metal at a temperature of $30\,°C$ its value is:

  $$M = \frac{v_{inlet}}{v_{sound}} = 0.018.$$

Taking into account that the speed of sound in molten liquids is higher (of 4200 m/s for liquid Fe, see [16]), the Mach number is quite low for both phases, so the fluid can be considered incompressible with constant density.

• Froude number, Fr, gives the relation between inertia and gravity terms:

$$Fr = \frac{v_{inlet}^2}{gd} = 67.21,$$

where g (m/s^2) is the gravitational acceleration. The value of Fr is bigger than 1, so inertia forces of the hot metal jet overcome those of the gravity near the taphole. As the fluid leaves the taphole, the characteristic length increases and Froude number decreases. Therefore, gravity forces overcome inertia ones. So, the fluid describes a parabolic path.

• Reynolds number, Re, gives the relation between inertia and viscosity terms:

$$Re = \frac{\rho_h v_{inlet} d}{\mu_h} = 3.7E + 05.$$

The value of Re is quite high and consequently, a turbulent flow must be considered.

• To study surface tension importance in turbulent flows, Weber number, We, must be analysed. It gives the relation between inertia and surface tension terms:

$$We = \frac{\rho_h d v_{inlet}^2}{\sigma_{h,a}} = 1.23E + 04,$$

where $\sigma_{h,a}$ (N/m) is the surface tension coefficient between hot metal and air, whose value is $\sigma_{h,a} = 1.25$ N/m. Since Weber number is quite high, hot metal jet inertia overcomes its surface tension with the air.

After this dimensionless analysis, we can conclude that the hot metal jet running out of the blast furnace consists of a transient problem for an incompressible, turbulent and multiphase flow, where surface tension forces do not play an important role. However, surface tension will be included in the mathematical model in order to achieve an accurate numerical simulation of the interaction between the jet and the thin pool of fluid reposing over the runner.

Before introducing the mathematical model associated to jet behaviour, a previous analysis is included in the next section. It allows to answer two main questions: the relevant physical magnitude to characterize the runner wear and the most suitable choice of turbulence model. Once these doubts are clarified, in Section 4 we proceed to present the mathematical model for the hot metal jet numerical simulation.

3. Previous analysis based on benchmark tests

In this section we analyze the main erosion mechanisms, the magnitudes involved, and the more appropriated hydrodynamic models to carry out an accurate simulation of the actual jet impact. In Subsection 3.1, shear stress is identified as the main mechanical parameter responsible of running wear. In Subsection 3.2, three benchmark laboratory tests, introduced in [1] and [17], are included. An improvement of the classical formula given in [1] is proposed in Subsection 3.3. In Subsection 3.4, a discussion of the most suitable turbulence model in order to compute shear stress produced by a turbulent jet impacting over a rigid wall is included. For that, we analyze two turbulence models to simulate the physical experiments performed by [1]. The results show that Shear Stress Transport (SST) $k - \omega$ turbulence model is the best choice. This section is completed with the validation of the proposed formula for the calculation of the shear stress on three numerical tests in Subsection 3.5.
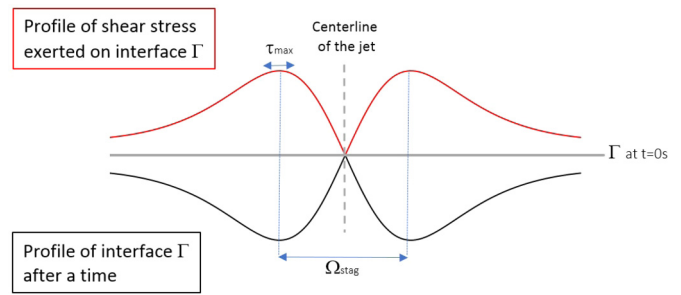

Fig. 3. Upper curve: Profile of the shear stress exerted by a jet impacting normally on the solid-fluid interface Γ. Lower curve: Profile of the theoretical modification of solid-fluid interface, Γ, according to classical erosion law, (1) or (2).

3.1. Mechanical erosion mechanisms

In this section some erosion laws collected in the literature are analyzed in order to identify the mechanical parameters responsible of runner wear.

As the runner is made of refractory concrete, we focus on the erosion on a porous solid (runner) produced by a fluid (hot metal). In this field, a large number of empirical and semi-empirical erosion laws and models have been developed, but their application is restricted to very specific scenarios.

An erosion law that is applicable to our problem is the shear stress excess law, also known as classical erosion law, proposed by [11]. This law relates the eroded mass flux, $\dot{m}$ (kg/(m^2 s)), with the shear stress excess, $(\tau - \tau_c)$ (Pa), exerted on the solid-fluid interface, Γ:

$$\dot{m} = \begin{cases} k_{er}(\tau - \tau_c), & \text{if } \tau > \tau_c, \\ 0, & \text{otherwise,} \end{cases} \quad \text{on } \Gamma, \tag{1}$$

being τ_c (Pa) the critical shear stress, from which the erosion takes place, and k_{er} (s/m) the erosion kinetics coefficient. Both, τ_c and k_{er}, only depend on the porous material.

Eroded mass flux can be written in terms of the solid-fluid interface modification velocity, v_Γ (m/s):

$$\dot{m} = v_\Gamma \rho_s \quad \text{on } \Gamma,$$

being ρ_s (kg/m^3) the porous solid density. So, classical erosion law can be also written as

$$v_\Gamma = \begin{cases} k_d(\tau - \tau_c), & \text{if } \tau > \tau_c, \\ 0, & \text{otherwise,} \end{cases} \quad \text{on } \Gamma, \tag{2}$$

with $k_d = k_{er}/\rho_s$.

It is well known that the centerline of a jet has null velocity at the impact point, as well as null shear stress. As we move away from this point, these magnitudes increase until they reach a maximum, τ_{max} (Pa), and then they decrease again. So, if we look at the center plane of a jet with normal impact over a wall, we can see two symmetrical maxima and a minimum in between, see Fig. 3. The area between the two maxima is called stagnation zone, Ω_{stag}. Notice that the application of classical erosion laws, (1) or (2), translates into a peak of non-eroded material, as shown in Fig. 3, what in practice is not observed.

To overcome this difficulty, [13] recently introduced the following modification to the classical erosion law:

$$v_\Gamma = \begin{cases} k_d(\tau_{max} - \tau_c), & \text{if } \tau_{max} > \tau_c \text{ in } \Omega_{stag}, \\ k_d(\tau - \tau_c), & \text{if } \tau > \tau_c \text{ out of } \Omega_{stag}, \\ 0, & \text{otherwise,} \end{cases} \quad \text{on } \Gamma.$$

Since most of the bibliography erosion laws point the shear stress as the responsible for the mechanical erosion process, this one is the magnitude selected to focus on and its accurate computation is the objective of the following subsections.
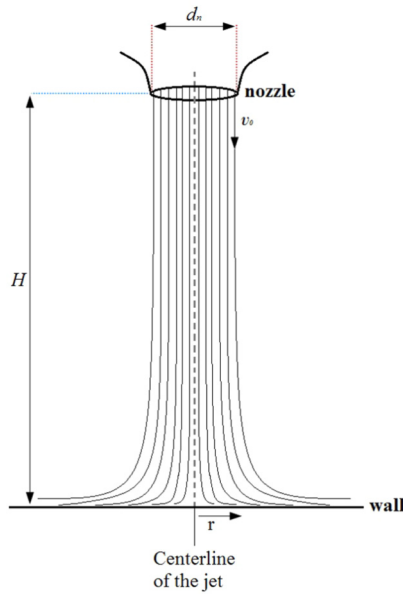
Fig. 4. Scheme of a normal circular jet impacting over a wall.

Table 2

Data of the experimental setup for experiments performed by [1] and [17].

Experiment	H (mm)	d_n (mm)	v_0 (m/s)
BR-RUN No. 4	496.062	23.444	50.630
BR-RUN No. 5	422.275	6.426	89.365
BL	457.2	25.4	106.75

3.2. Benchmark laboratory tests

In order to choose the most suitable turbulence model for studying shear stress exerted by a jet over a rigid wall, we analyse the results of simulating three laboratory experiments: two performed by [1], more precisely those named *BR RUN No. 4* and *BR RUN No. 5*, and one by [17], identified in the following by the *BL* acronym.

These experiments consist on a circular turbulent jet composed by air, being d_n (mm) the nozzle diameter, from which the fluid goes down at a velocity v_0 (m/s) and impacts normally over a rigid wall placed at a distance H (mm) from the nozzle, see Fig. 4. Data of the experimental setup are shown in Table 2.

In [1], experimental measurements are presented as well as their adjustment equation for the shear stress exerted over the wall, τ (Pa), which are normalized by the maximum shear stress, τ_{max} (Pa). A formula to approximate the maximum shear stress is also deduced. The adjustment equation they got is

$$\frac{\tau}{\tau_{max}} = 0.18 \left(\frac{1 - e^{-114\lambda^2}}{\lambda} \right) - 9.43 \lambda e^{-114\lambda^2}, \quad (3)$$

where λ is an adimensional parameter defined as $\lambda = r/H$, being r (mm) the distance to the jet center over the wall (see Fig. 4). Besides, maximum shear stress was approximated by:

$$\tau_{max} = 0.16 \frac{\rho_f v_0^2}{\left(\frac{H}{d_n} \right)^2}, \quad (4)$$

where $\rho_f = 1.225$ (Kg/m^3) is the fluid mass density. In their work, maximum shear stress was experimentally found at $\lambda_{max} \approx 0.14$. For their shear stress adjustment equation, they also used the data obtained by [17]. Experimental data and adjustment curve, given by equation (3), are shown in Fig. 11 of [1]. There it is quite visible how the adjustment curve fits well for low values of λ, but it does not for high values. Although equation (3) was criticized by other authors, see for example [18], the agreement among shear measurements for impinging jets
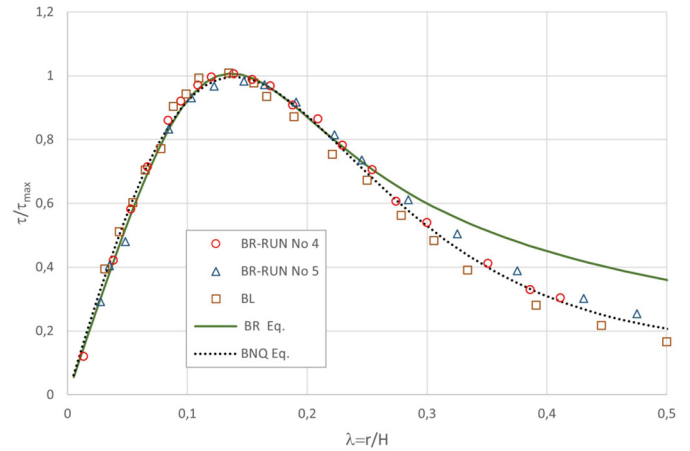

Fig. 5. Experimental data obtained by [1] and by [17], together with the adjustment equation (3) and the improved adjustment equation (6).

that are fully developed is acceptable, even compared with other experiments, especially for small λ values. Notice that adjustment in equation (3) was introduced in the seventies, so it is totally normal to find some discrepancies, like the mentioned differences for high values of λ or the fact that the maximum value for τ/τ_{max} is 1.007 instead of the expected value 1, and that it occurs at $\lambda = 0.1371$ instead of 0.14. Nowadays we have access to much more precise adjustment tools without requiring too much complication. These reasons have led the authors to look for a new formula to adjust the experimental data. According to classical erosion law (1), if exerted shear stress for high values of λ is greater than critical shear stress of one material, this area should be eroded. So, it is important to propose a new adjustment equation to accurately approximate shear stress and therefore the subsequent wear. In order to improve their shear stress formula, experimental data were asked to Dr. N. Rajaratnam, but, unfortunately, the data collection was not available and he proposed us to recalculate the data points coordinates from Fig. 11 of their article. To achieve this goal, we used the free software **Engauge Digitizer** [19]. Using this software we localized the experimental points of that graphic for the three experiments, collected in Tables 3–5.

Fig. 5 shows the data of Tables 3–5 and the goodness of the adjustment given by equation (3) (identified with the BR acronym) for the three benchmark cases considered. Besides, we can see its agreement with Fig. 11 of [1].

3.3. Improved formula to calculate the normalized shear stress

This subsection has the objective of proposing a new adjustment equation by fitting the three benchmark experimental tests. Following the mathematical profile of the adjustment equation proposed by [1], the following non linear curve to fit the data of Tables 3–5 is proposed:

$$\frac{\tau}{\tau_{max}} = a \left(\frac{1 - e^{-b\lambda^2}}{\lambda} \right) - c \lambda e^{-d\lambda^2}, \quad (5)$$

where a, b, c and d are adjustment constants. Their computed values using MATLAB® are included in Table 6 for each experiment along with their average and information about the goodness of fit.

To propose the new adjustment shear stress equation, identified by the *BNQ* acronym, we use the average of the three computed values for each constant. *BNQ* normalized shear stress equation adjustment is the following one:

$$\frac{\tau}{\tau_{max}} = 0.2502 \left(\frac{1 - e^{-54.49\lambda^2}}{\lambda} \right) - 1.344 \lambda e^{-3.318\lambda^2}. \quad (6)$$

Table 3

Data obtained from Fig. 11 of [1] for the *BR-RUN No. 4* experiment.

λ	τ/τ_{max}	λ	τ/τ_{max}	λ	τ/τ_{max}	λ	τ/τ_{max}
0,01339	0,12089	0,09445	0,92072	0,16912	0,96832	0,27384	0,60710
0,03810	0,42174	0,10851	0,97103	0,18776	0,90817	0,29960	0,53967
0,05280	0,58277	0,11980	0,99640	0,20872	0,86532	0,35063	0,41244
0,06662	0,71514	0,13871	1,00688	0,22931	0,78237	0,38590	0,33022
0,08373	0,86102	0,15392	0,98855	0,25415	0,70536	0,41107	0,30475

Table 4

Data obtained from Fig. 11 of [1] for the *BR-RUN No. 5* experiment.

λ	τ/τ_{max}	λ	τ/τ_{max}	λ	τ/τ_{max}	λ	τ/τ_{max}
0,02758	0,29144	0,10342	0,9307	0,19057	0,91785	0,32527	0,50469
0,03484	0,4044	0,12225	0,9679	0,22259	0,81448	0,37532	0,38885
0,04835	0,4795	0,14730	0,9825	0,24554	0,73547	0,43049	0,30189
0,08428	0,83243	0,16438	0,9719	0,28425	0,61143	0,47513	0,25449

Table 5

Data obtained from Fig. 11 of [1] for the *BL* experiment.

λ	τ/τ_{max}	λ	τ/τ_{max}	λ	τ/τ_{max}	λ	τ/τ_{max}
0,03108	0,39467	0,08834	0,90419	0,16614	0,93477	0,30568	0,48368
0,04329	0,51169	0,09888	0,94288	0,18905	0,87198	0,33364	0,39155
0,05440	0,60194	0,10963	0,99304	0,22087	0,75428	0,39077	0,28084
0,06476	0,70455	0,13445	1,00858	0,24998	0,67271	0,44540	0,21771
0,07783	0,77199	0,15537	0,97717	0,27847	0,56248	0,50000	0,16603

Table 6

Values of constants obtained from fitting Eq. (5). SSE is the sum square of residuals and R^2 measures the success of the fit, being 1 its ideal value.

Experiment	a	b	c	d	SSE	R^2
BR-RUN No. 4	0.2586	53.54	1.485	3.663	0.0048	0.996
BR-RUN No. 5	0.2525	51.24	1.197	3.196	0.0041	0.996
BL	0.2395	58.69	1.351	3.094	0.0056	0.996
Average	0.2502	54.49	1.344	3.318		

The plot of the experimental data points together with *BR* adjustment equation (3) and *BNQ* adjustment equation (6) is shown in Fig. 5. We can observe that the new one fits very well, even for high values of λ.

3.4. Turbulence model choice

In order to carry out the numerical simulation of both experiments, in what follows, a steady problem is solved. Taking into account the axial symmetry of a normal circular jet, the simulations are performed using a two-dimensional domain, $\Omega_e = [0, L_w] \times [0, H]$, being L_w the length of the wall segment considered for the simulation. This length is chosen long enough so that the numerical results are not affected by the condition imposed on the right boundary of the computational domain; a value of $L_w = 250$ mm is assumed for both experiments. The software used for the simulations is ANSYS Fluent®, version 15.0.

The boundaries of the geometry shown in Fig. 6 are the following:

- Γ_{axis} ($r = 0$ mm and $z \in (0, H)$) corresponds to the jet axis.
- Γ_{in} ($r \in (0, d_n/2)$ and $z = H$), corresponds to the boundary through which the air gets into the domain at the velocity v_0.
- Γ_{out} ($r \in (d_n/2, L_w)$ and $z = H$) $\cup$ ($r = L_w$ and $z \in (0, H)$), is a fictitious boundary considered to be open air. A pressure outlet condition is imposed on it.
- Γ_{wall} ($r \in (0, L_w)$ and $z = 0$ mm) is the wall segment where the air jet impacts and shear stress is developed.

Since our intention is to analyze shear stress on the wall, it is necessary to choose a turbulence model for an accurate treatment of boundary layer effects. In the following, two different turbulence models are compared: Standard $k - \omega$, proposed by [10], and one of its variants, Shear Stress Transport (SST) $k - \omega$ model, proposed by [20]. The rea-
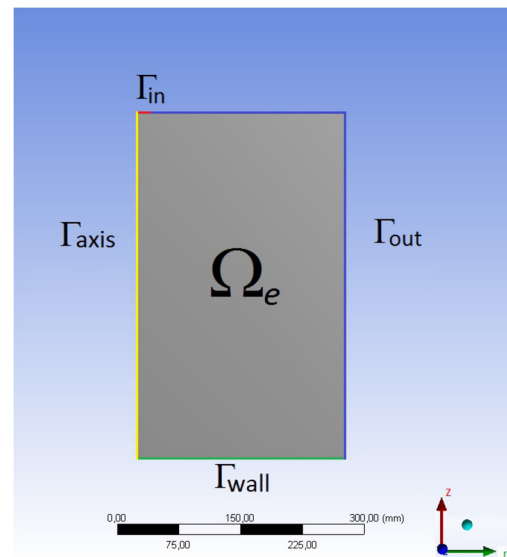
Fig. 6. Computational domain Ω_e considered for the simulation of the experiments performed in [1].

sons for this election are two: the first one is that Standard $k - \omega$ model[1] was developed for wall-bounded shear flows, and the second one arises from the PhD thesis of [12], who concluded that, as time progresses, Standard $k - \omega$ model provides better results than Standard $k - \epsilon$ model (one of the most common turbulence models, developed for free shear flows); similar conclusions are reported in [21]. The main difference between the Standard $k - \omega$ and the SST $k - \omega$ turbulence models is that the last one combines the former near the walls with the Standard $k - \epsilon$ turbulence model far from them, and its use is recommended in predicting boundary layers under strong adverse pressure gradients (see [22]). As will be seen in this work, the profiles of the shear stress exerted by the pressurized air and hot metal jets are very similar, except for the lack of symmetry with respect to the centre of the jet, due to the discharge angle of the hot metal. Therefore, and given the unavailability of

---

[1] Abbreviation "Std." is used in graphics and tables to designate Standard $k - \omega$ turbulence model to save space.

Table 7

Characteristics of the meshes used for the simulation of the laboratory experiments presented in [1].

	Mesh 1		Mesh 2		Mesh 3	
Mapped	Yes		Yes		No	
Inflation	No		No		Yes	
Axis divisions	300		250		350	
Wall divisions	150 + *Bias Factor* 2		100 + *Bias Factor* 2		200 + *Bias Factor* 2	
RUN No.	*4*	*5*	*4*	*5*	*4*	*5*
No. elements	43,808	43,955	24,700	24,255	18,083	18,716

Table 8

Maximum shear stress values and the corresponding value of λ. The first column corresponds to the estimated values by Beltaos and Rajaratnam equation (4), and the following ones to those obtained by the numerical simulations.

	BR-RUN No. 4						
	BR Eq. (4)	Mesh 1		Mesh 2		Mesh 3	
		Std.	SST	Std.	SST	Std.	SST
τ_{max} (Pa)	1.122	2.916	1.166	2.567	1.051	2.215	1.042
λ	≈ 0.14	0.059	0.131	0.065	0.128	0.078	0.133
	BR-RUN No. 5						
	BR Eq. (4)	Mesh 1		Mesh 2		Mesh 3	
		Std.	SST	Std.	SST	Std.	SST
τ_{max} (Pa)	0.363	0.496	0.344	0.468	0.301	0.260	0.387
λ	≈ 0.14	0.093	0.157	0.101	0.146	0.087	0.140
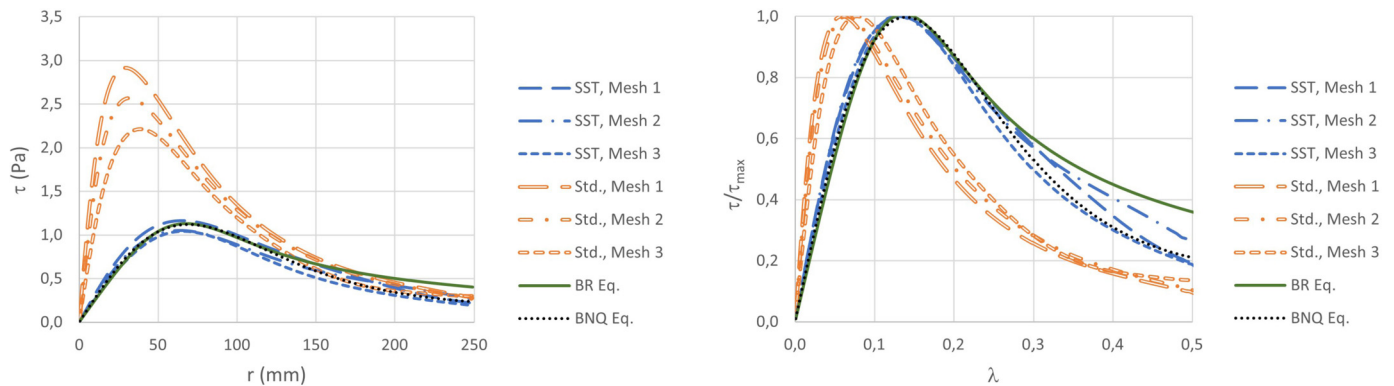
Fig. 7. Results of the *BR-RUN No. 4* simulations, using the three meshes shown in Table 7 and the Standard (Std.) and SST $k - \omega$ turbulence models. Left: Shear stresses exerted on the wall. Right: Normalized shear stresses.

experimental data for the hot metal, these benchmarks allow a proper evaluation of which of the methods will best capture the shear stress in the real case. In the numerical simulation, three different meshes are used, with the characteristics shown in Table 7. Term *Inflation* refers to a type of mesh refinement that generates layers of parallel elements on a surface (or line, in 2D). It is usually used near the walls when there is a boundary layer, as the case of the turbulent boundary layer. It is highly recommendable to use *inflations* when generating no mapped meshes, like in Mesh 3, where a refinement of 10 layers with a growth rate of 1.05 among them in 5 mm of total thickness is considered. *Bias Factor* is the ratio of the largest edge to the smallest one of the mesh.

The laboratory benchmark tests have been numerically reproduced using commercial software ANSYS Fluent®, version 15.0 for the three meshes. The results obtained are shown in Figs. 7 and 8. In spite of not having the shear stress experimental measures, we compare the results of the simulations with the shear stress calculated by equation (3) and their maximum value, calculated from equation (4). All shear stress curves have a minimum at $r = 0$ mm. This minimum corresponds to the impact point of the jet centerline, where the velocity is null, as well as shear stress, what is in good agreement with real observations. As we move away from this point, shear stress increases until reaching a maximum value and then decreases again as we have previously announced.

It is quite clear that the results obtained using the SST $k - \omega$ turbulence model are closer to those predicted by equation (4). Furthermore, the improved fitting curve introduced in (6) is closer to the results of the numerical simulations with the SST $k - \omega$ turbulence model than those obtained from (3), even for λ values far from the centre of the jet. In addition, in the Figs. 7 and 8, we can see how the Standard $k - \omega$ turbulence model overestimates the shear stress, and it is more dependent on the mesh than the SST $k - \omega$ turbulence model.

In Table 8 maximum shear stress values and the corresponding value of λ for each experiment, turbulence model and mesh are summarized. We can see how Mesh 3 provides good results for both experiments, in spite of being the most coarse of the three ones. The reason is the *Inflation* application, that allows to solve accurately the boundary layer.

In conclusion, to model the behaviour of the hot metal jet, the SST $k - \omega$ turbulence model seems to be the most appropriated. In Section 4, a detailed description of its associated mathematical model is presented.

3.5. Numerical validation of the shear stress calculation in other scenarios

To make sure that the new adjustment equation for normalized shear stress is verified in other scenarios of jet impact, three new numerical experiments are proposed. They are similar to those performed in the laboratory experiments described above, although the jet nozzle height, its diameter, and the output speed are modified. The values of H, d_n
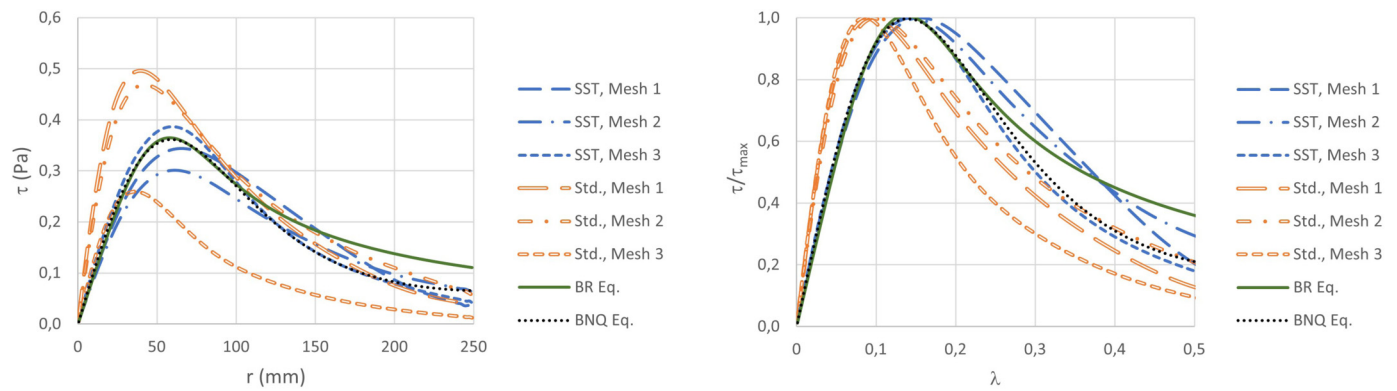
Fig. 8. Results of the *BR-RUN No. 5* simulations, using the three meshes shown in Table 7 and the Standard (Std.) and SST $k - \omega$ turbulence models. Left: Shear stresses exerted on the wall. Right: Normalized shear stresses.

Table 9
Details of the numerical experiments data performed to validate the new adjustment equation (5).

Experiment	H (mm)	d_n (mm)	v_0 (m/s)	No. elements
Exp. 1	500	20	50	18,026
Exp. 2	400	10	100	19,456
Exp. 3	350	20	60	22,931

and v_0 for each numerical experiment are shown in Table 9. The magnitude of these values incorporates substantial changes with respect to laboratory data, although the jets are still considered to be air. Notice that in these cases, physical experiments were not performed, but their simulation using the commercial software ANSYS Fluent® version 15.0.

For the numerical simulations, we have used the SST $k - \omega$ turbulence model. As done in the previous subsection, we consider the bidimensional domain described in Fig. 6 for the values given in Table 9, and perform each numerical experiment in steady regime using a mesh based on Mesh 3 specifications (see Table 7), such that the number of elements corresponds to the last column in Table 9 for each experiment.

Normalized shear stress obtained for the three trials as well as the adjustment curves proposed for *BR* and for us are shown in Fig. 9, for each performed simulation. The new normalized shear stress equation adjustment (6) fits very well the normalized numerical shear stress profile for the three numerical experiments. It also fits better than the classical formula (3) given by [1].

4. Mathematical model

In this section, we come back over the blast furnace jet problem introduced in Section 2. A complete mathematical model for an incompressible multiphase turbulent flow in transient regime is explained. After the analysis presented in Subsection 3.4, SST $k - \omega$ turbulence model is considered for the turbulence problem. The multiphase problem is solved by applying the Volume of Fluid (VOF) method and the Continuum Surface Force (CSF) model.

For sake of simplicity, we consider the bidimensional problem posed on the longitudinal central section of the runner, inside the area marked with dash-line in Fig. 2. Computational domain Ω is presented in Fig. 10, and their boundaries are:

- Γ_{in} corresponds to the end of the taphole, through which fluids run out from the blast furnace and enter the computational domain. It is placed 1.27 m above the bottom runner surface and has a diameter of 0.06 m.
- Γ_{out} is the part in contact with the air. It is a fictitious boundary, which is considered far enough from the jet in order to not to affect its numerical simulation.

- Γ_{wall} corresponds to the bottom runner surface, defined by the points: (0, 0.8), (0.615, 0.8), (1.615, 0.07) and (15.965, 0), and its final vertical wall.

4.1. Incompressible model

An incompressible flow behaviour in laminar regime under the force of gravity is described by Navier-Stokes equations for mass and momentum balances:

$$
\begin{cases}
\text{div } \mathbf{v} = 0, \\
\rho_f \dfrac{\partial \mathbf{v}}{\partial t} + \rho_f \text{div}(\mathbf{v} \otimes \mathbf{v}) + \text{grad} \pi - 2\mu_f \text{div}(\mathbf{D}(\mathbf{v})) = \rho_f \mathbf{g},
\end{cases}
\tag{7}
$$

where $\mathbf{v}$ (m/s) is the flow velocity, $\mathbf{D}(\mathbf{v})$ (s^{-1}) is the symmetrical part of its gradient, π (Pa) is the flow pressure, μ_f (Pa s) is the fluid dynamic viscosity, t (s) is the time and $\mathbf{g}$ (m/s^2) is the gravitational acceleration vector. Operator $\otimes$ denotes tensor product of two vectors. For more details, see for example [23].

4.2. Turbulence model

Turbulent flows are developed in very different size scales and a direct numerical simulation would be extremely expensive from a computational point of view. So, magnitudes of interest (for example, the velocity $\mathbf{v}$) are usually decomposed into their mean value (denoted by $\mathbf{V}$ or $\langle \mathbf{v} \rangle$) and their fluctuation ($\mathbf{v}'$):

$$\mathbf{v} = \mathbf{V} + \mathbf{v}'.$$

Decomposed magnitudes are replaced in Navier-Stokes equations, (7), and the resulting equations are averaged, obtaining the following ones:

$$
\begin{cases}
\text{div} \mathbf{V} = 0, \\
\rho_f \dfrac{\partial \mathbf{V}}{\partial t} + \rho_f \text{div}(\mathbf{V} \otimes \mathbf{V}) + \rho_f \text{div}(\langle \mathbf{v}' \otimes \mathbf{v}' \rangle) + \text{grad} \Pi - 2\mu_f \text{div}(\mathbf{D}(\mathbf{V})) \\
\quad = \rho_f \mathbf{g},
\end{cases}
\tag{8}
$$

where operator Π (Pa) denotes the mean pressure [23]. It must be observed that averaged equations are analogous to those for a laminar incompressible flow, (7), in terms of averaged velocity and gradient. There is only a new term, proportional to the tensor product of velocity fluctuations, named Reynolds stress tensor (τ^R):

$$\tau^R = -\rho_f \langle \mathbf{v}' \otimes \mathbf{v}' \rangle.$$

This term introduces six new unknowns, while the number of equations remains the same. To overcome this situation, it is necessary to introduce the turbulence model.
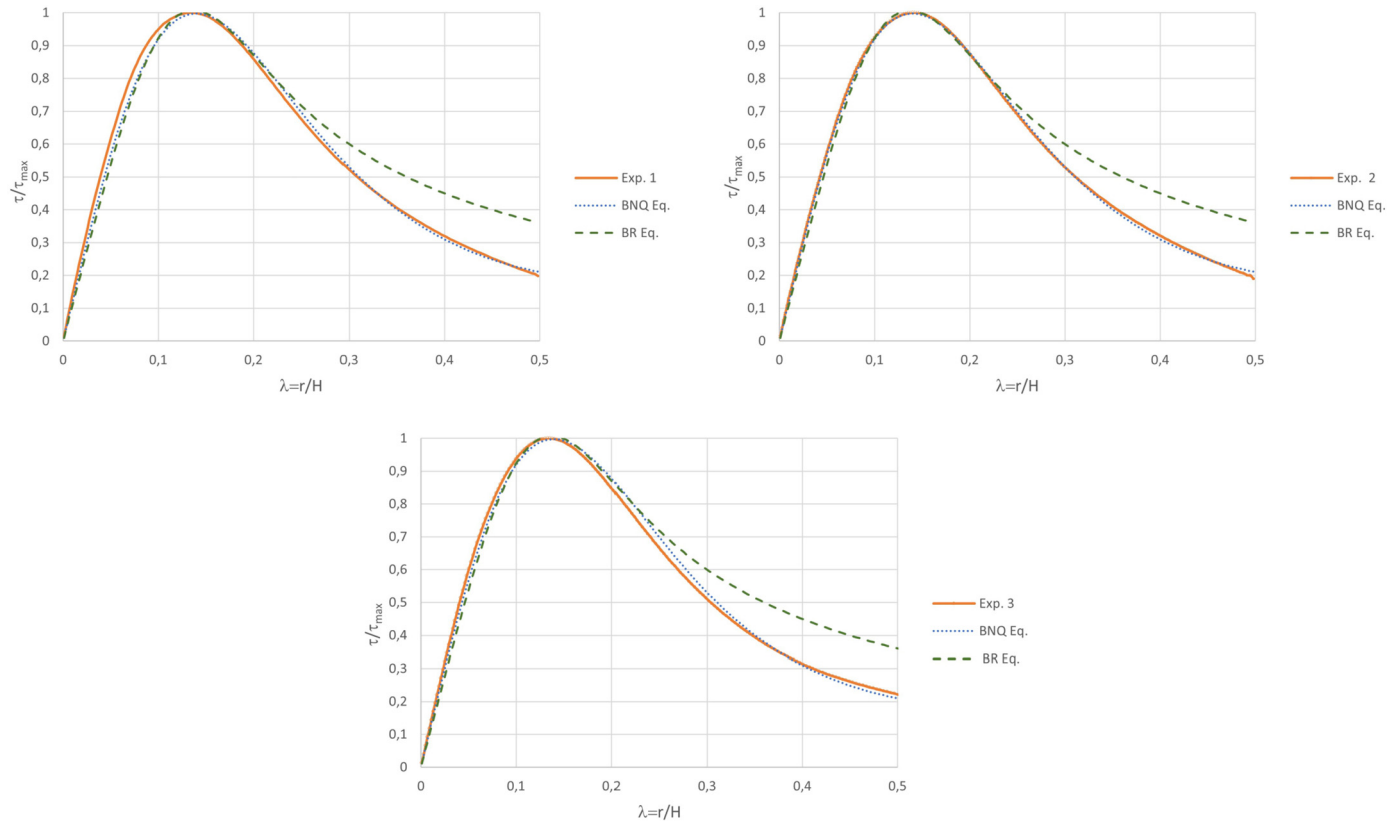
Fig. 9. Normalized shear stress for numerical experiments using the SST $k - \omega$ turbulence models. Top left: *Exp. 1*. Top right: *Exp. 2*. Bottom: *Exp. 3*.
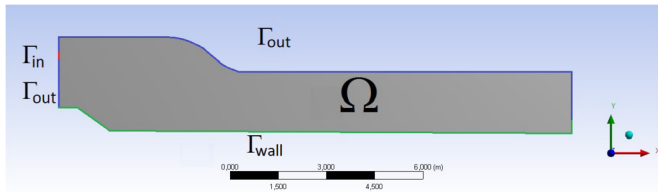

Fig. 10. Computational domain Ω for jet impact problem.

The Shear Stress Transport (SST) $k - \omega$ turbulence model is within the first order Reynolds Averaged Navier Stokes (RANS) models. These models use Boussinesq hypothesis to approximate the Reynolds stress tensor. According to this hypothesis, this tensor is assumed to be similar to viscous stress tensor:

$$\boldsymbol{\tau}^R = 2\mu_T \mathbf{D}(\mathbf{V}) + \frac{1}{3}\mathrm{tr}(\boldsymbol{\tau}^R)\mathbf{I},$$

being μ_T (Pa s) the turbulent dynamic viscosity and $\mathbf{I}$ the identity matrix. This expression corresponds to the decomposition of a tensor into its deviatoric and spherical parts, being the deviatoric part proportional to $\mathbf{D}(\mathbf{V})$, with a proportionality factor of $2\mu_T$. The spherical part is related to the turbulence kinetic energy k (m^2/s^2), that is defined as

$$k = \frac{1}{2}\langle |\mathbf{v}'|^2 \rangle = -\frac{1}{2\rho_f}\mathrm{tr}(\boldsymbol{\tau}^R).$$

Taking into account these assumptions, averaged Navier-Stokes equations presented in (8) can be written as:

$$\begin{cases} \mathrm{div}\mathbf{V} = 0, \\ \rho_f \frac{\partial \mathbf{V}}{\partial t} + \rho_f \mathrm{div}(\mathbf{V} \otimes \mathbf{V}) + \mathrm{grad}\Pi^* - 2\mu_{eff}\mathrm{div}(\mathbf{D}(\mathbf{V})) = \rho_f \mathbf{g}, \end{cases} \quad (9)$$

where $\Pi^* = \Pi - \mathrm{tr}(\boldsymbol{\tau}^R)\mathbf{I}/3$ is the reduced mean pressure, and $\mu_{eff} = \mu_f + \mu_T$ is the effective dynamic viscosity.

In addition, SST $k - \omega$ turbulence model consists of two transport equations that have the objective of finding the turbulent dynamic viscosity, μ_T [20]. One equation is proposed for k and another one for the specific turbulence dissipation rate, ω (1/s), that is proportional to $\frac{\rho_f k}{\mu_T}$ through the relation:

$$\mu_T = \frac{1}{A}\frac{\rho_f k}{\omega},$$

where A is a function computed as:

$$A = \max\left[\frac{1}{\alpha^*}, \frac{S F_2}{a_1 \omega}\right],$$

being α^* and a_1 model constants experimentally obtained, S (1/s) the strain rate magnitude, and F_2 a blending function that depends on variables k and ω, fluid properties, and the vertical distance to the wall. Notice that this function allows to switch from Standard $k - \omega$ turbulence model formulation to Standard $k - \varepsilon$ one, and vice versa, depending on the distance to the wall [20].

Transport equations for k and ω are the following:

$$\begin{cases} \rho_f \frac{\partial k}{\partial t} + \rho_f \mathbf{V} \cdot \mathrm{grad}k = \mathrm{div}(\Gamma_k \mathrm{grad}k) + G_k - Y_k, \\ \rho_f \frac{\partial \omega}{\partial t} + \rho_f \mathbf{V} \cdot \mathrm{grad}\omega = \mathrm{div}(\Gamma_\omega \mathrm{grad}\omega) + G_\omega - Y_\omega + D_\omega, \end{cases} \quad (10)$$

where Γ_k (kg/ms) and Γ_ω (kg/ms) are the effective diffusivity terms of k and ω, G_k (kg/ms^3) and G_ω (kg/m^3 s^2) are the generation terms of k and ω, Y_k (kg/ms^3) and Y_ω (kg/m^3 s^2) are the dissipation terms of k and ω due to turbulence, and D_ω (kg/m^3 s^2) is the cross-diffusion term, that depends on k and ω gradients. These terms have the following expressions:

$$\Gamma_k = \mu_f + \frac{\mu_T}{\sigma_k}, \quad \Gamma_\omega = \mu_f + \frac{\mu_T}{\sigma_\omega},$$

$$G_k = \mu_T |\mathbf{D}(\mathbf{V})|, \quad G_\omega = \alpha \frac{\rho_f}{\mu_T} G_k,$$

$$Y_k = \rho_f \beta^* k\omega, \quad Y_\omega = \rho_f \beta\omega^2 \quad \text{and}$$

$$D_\omega = 2(1 - F_1)\rho_f \frac{1}{\omega\sigma_{\omega,2}} \text{grad} k \cdot \text{grad}\omega,$$

where α and $\sigma_{\omega,2}$ are model constants experimentally obtained, β and β^* are functions experimentally adjusted, σ_k and σ_ω are the Prandtl numbers for k and ω, respectively, and F_1 is another blending function. Notice that F_1, like function F_2, depends on variables k and ω, fluid properties, and the vertical distance to the wall. See [20] for more details.

4.3. Multiphase model for inmiscible fluids

Since our main target is the numerical simulation of the jet impact, we have chosen a direct multiphase numerical method in which the interface between two different fluids is resolved and it is free to move, deform, breakup and coalesce. In particular, in Section 5 we propose the Volume of Fluid (VOF) method, which is the most well-known and widely used direct multiphase method. This method uses the volume fraction function or the so-called colour function that represents the fraction of each phase. The continuous mathematical modelling presented in this section is oriented to the above-mentioned numerical procedure. For sake of simplicity, multiphase model for a laminar flow is presented. The generalization to the turbulence multiphase model is presented in next subsection.

Previously to write continuum balance equations for a multiphase flow, it is necessary to write them for just one phase p. For this, using the notations introduced by [24], some definitions are given.

Let $B(r, \mathbf{x})$ be a ball of radius r centered at $\mathbf{x}$, $\text{Vol}(B(r, \mathbf{x}))$ its volume, and $\text{Vol}_p(B(r, \mathbf{x}), t)$ the volume of phase p inside B at time t. Then, the ratio of volume of phase p to total volume in the ball B at each time t is defined as:

$$A_p(r, \mathbf{x}, t) = \frac{\text{Vol}_p(B(r, \mathbf{x}), t)}{\text{Vol}(B(r, \mathbf{x}))}.$$

This expression can be used for defining continuum variable $\alpha_p(\mathbf{x}, t)$:

$$\alpha_p(\mathbf{x}, t) = \lim_{r \to 0} A_p(r, \mathbf{x}, t),$$

that represents the volume fraction of phase p at point $\mathbf{x}$ and time t. We assume that these limiting processes make sense; a detailed analysis can be seen in [24]. Notice that the sum of volume fractions of all phases at $\mathbf{x}$ is the unity. Given any t, if there exists a radius r_0, such that for all $r \leq r_0$, $B(r, \mathbf{x})$ is completely occupied by phase p its volume fraction $\alpha_p(\mathbf{x}, t) = 1$, whereas if $B(r, \mathbf{x})$ is completely occupied by other phases then $\alpha_p(\mathbf{x}, t) = 0$. The phase interface location is thus interpreted somewhere with volume fraction function value between these limits.

Assuming that there is no production of mass of any phase due to change of phase or chemical reaction, continuum mass and momentum balance equations of phase p are written in terms of its variables (denoted with subscript p) as

$$\frac{\partial(\alpha_p\rho_p)}{\partial t} + \text{div}(\alpha_p\rho_p\mathbf{v}_p) = 0, \tag{11}$$

$$\frac{\partial(\alpha_p\rho_p\mathbf{v}_p)}{\partial t} + \text{div}(\alpha_p\rho_p\mathbf{v}_p \otimes \mathbf{v}_p) = \text{div}(\alpha_p\mathbf{T}_p) + \alpha_p\rho_p\mathbf{b}_p + \mathbf{M}_p, \tag{12}$$

where ρ_p (kg/m³) is the mass of phase p per unit of volume of constituent p, assumed to be constant; $\mathbf{v}_p$ (m/s) is the velocity of phase p; $\mathbf{T}_p$ (Pa) is the stress tensor for phase p; $\mathbf{b}_p$ (m/s²) is the body force per unit of mass acting on phase p and $\mathbf{M}_p$ (N/m³) is the force per unit of volume on phase p due to interaction with other phases. See [24] for more details.

Continuum effective mass density is defined for whole multiphase system in basis of each phase density and volume fraction:

$$\rho(\mathbf{x}, t) = \sum_p \alpha_p(\mathbf{x}, t)\rho_p. \tag{13}$$

Analogously, effective velocity or center-of-mass velocity, $\mathbf{v}(\mathbf{x}, t)$, and effective body force per unit of mass, $\mathbf{b}(\mathbf{x}, t)$, are defined for the whole multiphase system as the solution of:

$$\rho\mathbf{v} = \sum_p \alpha_p\rho_p\mathbf{v}_p \quad \text{and} \quad \rho\mathbf{b} = \sum_p \alpha_p\rho_p\mathbf{b}_p,$$

respectively. The effective stress tensor is defined by:

$$\mathbf{T} = \rho\mathbf{v} \otimes \mathbf{v} + \sum_p (\alpha_p\mathbf{T}_p - \alpha_p\rho_p\mathbf{v}_p \otimes \mathbf{v}_p).$$

After a sum over each phase p for equations (11) and (12), and using definitions above, equivalent single-field mass conservation and momentum conservation equations for the whole domain can be written as:

$$\begin{cases} \dfrac{\partial\rho}{\partial t} + \text{div}(\rho\mathbf{v}) = 0, \\ \dfrac{\partial(\rho\mathbf{v})}{\partial t} + \text{div}(\rho\mathbf{v} \otimes \mathbf{v}) = \text{div}(\mathbf{T}) + \rho\mathbf{b} + \mathbf{m}^\sigma. \end{cases} \tag{14}$$

Notice that summation of all $\mathbf{M}_p$ is assumed to be null inside each phase due to action-reaction principle. However, it is not null at the interface between different phases due to dynamic boundary condition stating the equilibrium of pressure and viscous stresses with the surface tension forces at the interface. Therefore, assuming that surface tension coefficient, σ (N/m), is constant between each two phases and a condition of zero tangential stress at the interface, the sum of all $\mathbf{M}_p$ is a magnitude called surface tension vector $\mathbf{m}^\sigma$ (N/m³). This vector consists on a term multiplied by a Dirac delta, so that it is not null only at the interface between two phases:

$$\mathbf{m}^\sigma = -\sigma\kappa\hat{\mathbf{n}}\delta(\mathbf{x} - \mathbf{x}_i, t),$$

where $\mathbf{x}_i$ denotes the interface points, $\delta(\mathbf{x} - \mathbf{x}_i, t)$ is the Dirac delta function at the interface at time t, κ (1/m²) is the interface mean curvature and $\hat{\mathbf{n}}$ is the unit normal vector to the interface, which is exterior to the p phase. The idea of defining this surface tension vector and its introduction into the momentum balance equation as a source term is called Continuum Surface Force model (CSF) and it was proposed by [15,25].

In practice the main difficulty to discretize model (14) is the accurate computation of the sharp interfacial shape and its properties, such as curvature. In the CSF model frame these magnitudes are computed as:

$$\kappa = \nabla \cdot \hat{\mathbf{n}}, \quad \hat{\mathbf{n}} = -\frac{\nabla\alpha_p}{|\nabla\alpha_p|} \quad \text{and} \quad \delta = |\nabla\alpha_p|.$$

Notice that the multiphase mass and momentum conservation equations (14) have the same conservation form as for single-phase flow but the single-phase density, velocity, stress and body forces are replaced by the effective mixture density, the center-of-mass velocity, the effective stress tensor and the effective body force, respectively.

To complete model (14), and taken into account that the total derivative of each phase volume fraction must remain null, the following additional equation is included:

$$\frac{\partial\alpha_p}{\partial t} + \mathbf{v}_p \cdot \text{grad}(\alpha_p) = 0, \quad 1 \leq p \leq N_p. \tag{15}$$

Since the phases are well separated, we consider the homogeneous model, which is the most simple within the continuous approach; it considers that the fluids are in mechanical equilibrium, assuming that the phases move with the same velocity at the interfaces [26], so for tracking the volume fraction equation (15) can be replaced by:

$$\frac{\partial\alpha_p}{\partial t} + \mathbf{v} \cdot \text{grad}(\alpha_p) = 0, \quad 1 \leq p \leq N_p. \tag{16}$$

4.4. Complete mathematical model

Once incompressible, turbulence and multiphase models have been introduced, in this section we write a complete system of equations to describe the incompressible, turbulent multiphase flow over the whole domain. Boundary and initial conditions for the actual jet impact problem with a fluid pool over the runner, are also presented.

For our purpose, we introduce the multiphase model for N_p immiscible phases, assuming that each of them obeys averaged Navier-Stokes equations (9) and SST $k - \omega$ turbulence model (10). Therefore, the system of equations considered for both cases over the whole domain Ω is the following:

$$
\begin{cases}
\text{div}\mathbf{V} = 0, \\
\rho \dfrac{\partial \mathbf{V}}{\partial t} + \rho \text{div}(\mathbf{V} \otimes \mathbf{V}) + \text{grad}\Pi^* - 2\mu_{eff}\text{div}(\mathbf{D}(\mathbf{V})) = \rho\mathbf{g} + \mathbf{m}^\sigma, \\
\rho \dfrac{\partial k}{\partial t} + \rho \mathbf{V} \cdot \text{grad}k = \text{div}(\Gamma_k \text{grad}k) + G_k - Y_k, \\
\rho \dfrac{\partial \omega}{\partial t} + \rho \mathbf{V} \cdot \text{grad}\omega = \text{div}(\Gamma_\omega \text{grad}\omega) + G_\omega - Y_\omega + D_\omega, \\
\mu_T = \dfrac{1}{A} \dfrac{\rho k}{\omega},
\end{cases}
\tag{17}
$$

where the first two equations correspond to the averaged Navier-Stokes equations for a turbulent incompressible flow (9), and last three equations correspond to the SST $k - \omega$ turbulence model [20]. It must be taken into account that the mass density appearing here is the continuum effective mass density, defined in (13); analogously the dynamic and turbulent viscosities appearing in (17) are the corresponding continuum effective magnitudes.

System of equations (17) is coupled with continuity mass equation for $\alpha_p(\mathbf{x}, t)$, (16):

$$
\frac{\partial}{\partial t}\alpha_p + \mathbf{V} \cdot \text{grad}(\alpha_p) = 0,
\tag{18}
$$

where the mean value $\mathbf{V}$ is used instead of $\mathbf{v}$.

The most critical case, from the shear stress point of view, is the first tapping of the blast furnace over each new working lining. Notice that in this case just gas-liquid two phases are involved, $N_p = 2$, so that $p = 1$ corresponds to air and $p = 2$ corresponds to hot metal.

4.4.1. Boundary conditions

Concerning to the boundary conditions (see Fig. 10) to complete the mathematical model (17) and (18), we assume the following:

- A **velocity inlet condition** is imposed on Γ_{in}, the end of the taphole through which hot metal enters the domain. Taking into account that just hot metal runs out through the taphole and that it has an inclination of 10°, we consider:

$$\mathbf{V}_{inlet} = v_{inlet}(\cos 10°, \sin 10°) \text{ and } \alpha_2 = 1$$

on Γ_{in}, for all time t.
Standard values are assumed for turbulent magnitudes: turbulent intensity, that is the relation between velocity fluctuation and mean velocity, has a value of 5%; eddy viscosity ratio, the relation between turbulent viscosity and molecular dynamic viscosity, is equal to 10. Then:

$$\mathbf{v}'_{inlet} = 0.05\mathbf{V}_{inlet}, \text{ and } \mu_{Tinlet} = 10\mu_h$$

on Γ_{in}, for all time t. Notice that μ_{Tinlet} corresponds to hot metal turbulence dynamic viscosity.
With these values, k and ω are calculated at the inlet as:

$$k_{inlet} = \frac{3}{2}(|\mathbf{v}'_{inlet}|)^2 \text{ and } \omega_{inlet} = \rho_h \frac{k_{inlet}}{\mu_{Tinlet}}$$

on Γ_{in}, for all time t.

- A **pressure outlet condition** is imposed on Γ_{out}, the fictitious boundaries considered to be open to the air. Since just air goes out through Γ_{out}, we consider:

$$\Pi = 0 \; Pa \text{ and } \alpha_2 = 0,$$

for all time t.
In addition, normal gradients of the flow variables are set to zero:

$$\frac{\partial \mathbf{V}}{\partial \mathbf{n}} = 0, \qquad \frac{\partial k}{\partial \mathbf{n}} = 0, \text{ and } \frac{\partial \omega}{\partial \mathbf{n}} = 0$$

on Γ_{out}, for all time t.

- A **no-slip wall condition** is imposed on Γ_{wall}, the rigid wall corresponding to the runner bottom surface. This means null velocity and turbulence kinetic energy on Γ_{wall}, for all time t. In $k - \omega$ turbulence models it is possible to solve the near-wall zone if the mesh is fine enough; in practice, wall laws are used to approximate the magnitudes [10]. We refer the interested reader to the Section 4.4.5 of the Theory Guide [27] of the software employed for further details about the standard no-slip condition. Besides, at this boundary, no materials transfer is considered, so that $\text{grad}(\alpha_p) \cdot \mathbf{n} = 0$ for $p = 1, 2$.

4.4.2. Initial conditions

Finally, null initial velocity and pressure fields are imposed over all the domain. Standard values are assumed for the turbulence magnitudes: $k = 1 \text{ m}^2/\text{s}^2$ and $\omega = 1 \text{ s}^{-1}$ in Ω at $t = 0$ s. For the first tapping of the blast furnace, since jet of hot metal is falling over dry concrete, hot metal volume fraction is imposed to be zero: $\alpha_2 = 0$ in Ω at $t = 0$ s.

5. Numerical simulation of the jet

The model described in Section 4 has been numerically solved with a finite volume method by using the software package ANSYS Fluent® 15.0. The discretization time scheme is first order implicit and the algorithm PRESTO! is used for pressure, so staggered grids are used. Volume of Fluid (VOF) method, used for the numerical simulation of multiphase problem, is linked to a discretization of the computational domain in finite volumes C_l, $1 \le l \le N_c$, being N_c the number of cells [28]. Volume fraction of phase p in cell C_l, $\alpha_p^l(t)$, is defined at each time as the average of continuum volume fraction, α_p, on the cell volume

$$\alpha_p^l(t) = \frac{1}{\text{Vol}(C_l)} \int_{C_l} \alpha_p(\mathbf{x}, t)dV_{\mathbf{x}}.$$

So, its possible values at time t are:

$$
\alpha_p^l = \begin{cases}
0, & \text{if cell } C_l \text{ is empty of phase } p, \\
1, & \text{if cell } C_l \text{ is full of phase } p, \\
\in (0, 1), & \text{if cell } C_l \text{ contains the interface between phase } p \text{ and another one.}
\end{cases}
$$

The computational domain is very extensive to try to follow the hot metal jet at any time; nevertheless, the jet has very small diameter with respect to domain area. Then, the standard discretization used in [9] involved a large number of mesh cells and, consequently, high computational costs. For these reasons, a dynamic adaptative mesh was used in this simulation, whose initial mesh was composed by 28,605 triangular and quadrangular cells. The adaptation of the mesh was defined in basis of the gradient of the hot metal jet volume fraction. This allowed to make the mesh finer only on the path of the jet, see Fig. 11. Time step considered was $\Delta t = 1E - 04$ s. In Fig. 11 the hot metal jet at different time steps is represented. We can also observe how the mesh is refined as the jet advances. At the end of the simulation (2.0 s) the mesh is composed by 110,604 elements.

The impact instant on the runner surface is identified at 0.78 s. At this time, shear stress exerted over the runner bottom surface is quite high, close to 4,000 Pa (see Fig. 13). Notice that shear stress on the
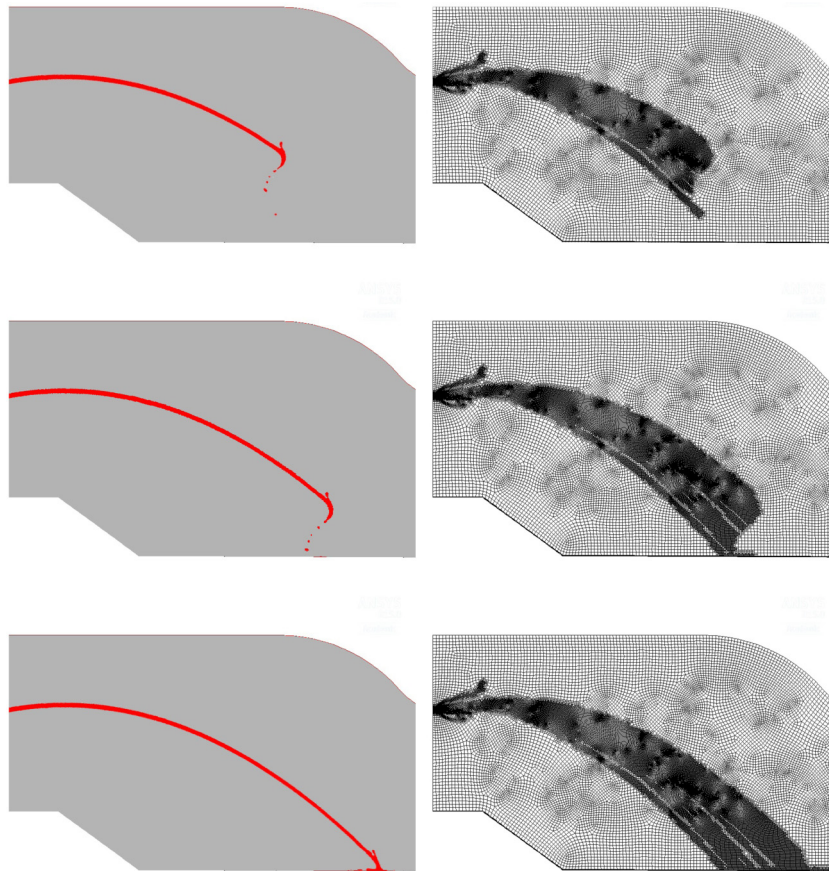
Fig. 11. Hot metal jet at 0.6 s, 0.7 s and 0.8 s, and corresponding meshes.
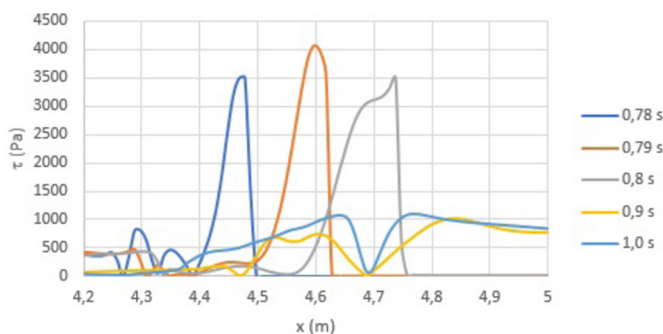

Fig. 12. Hot metal jet at 1.0 s.

Fig. 13. Shear stress vs distance from the taphole during the first time instants after the impact.
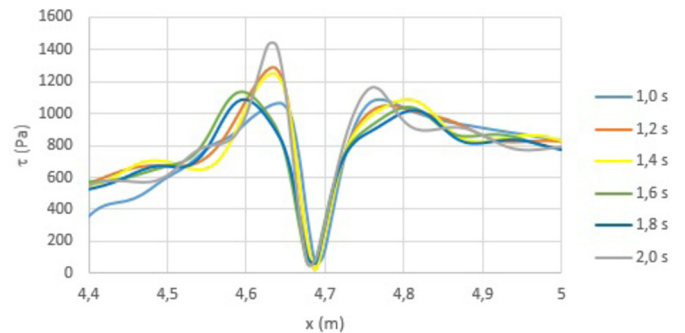

Fig. 14. Shear stress vs distance from the taphole after 1 s of casting.

The shear stress curves represented in Fig. 14 are in accordance with those obtained experimentally by [1] and numerically in Section 3.4. In those experiments they found two symmetrical maxima with respect to the center of the jet and a minimum between them. The minimum corresponded to the impact point of the centerline of the jet, as occurs in these numerical results. The reason why the maxima in our case (see Fig. 14) are not symmetrical is because the hot metal jet impacts with an angle different from 90°, which is the case in [1] and Section 3.4.

In order to determine the impact point, in Table 10 we represent the minimum shear stress on the impact area (τ_{min}) and the corresponding point, measured from the fluid inlet.

At the beginning of the process, pressure curves also fluctuate, see Fig. 15. But as time progresses, the curves overlap and the maximum is found at the same point for all of them, see Fig. 16 and Table 11. Notice that the impact point (located at a horizontal distance of 4.688 m from the fluid inlet), corresponds to the point with the maximum pressure and the minimum shear stress on the runner.

runner surface decrease with time due to the existence of liquid on the impact zone (see Fig. 12).

Fig. 13 allows us to analyze the evolution of the shear stress on the runner. It can be observed how after 0.9 s of casting two maximums and a minimum in between are being generated. As time progresses this shape becomes clearer (see Fig. 14).

Table 10
Minimum values of shear stress and the corresponding impact point.

t (s)	τ_{min} (Pa)	$x(\tau_{min})$ (m)
1.0	67.82	4.688
1.2	17.85	4.688
1.4	18.86	4.688
1.6	56.34	4.678
1.8	61.28	4.688
2.0	60.32	4.678
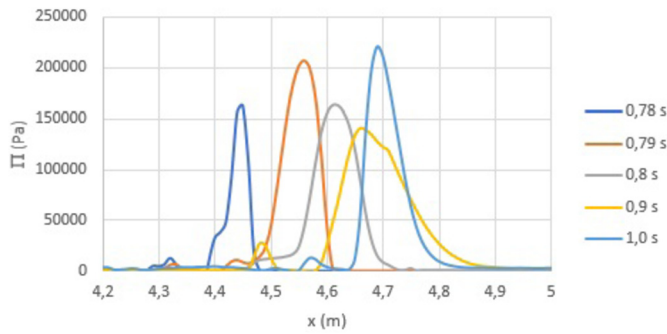
Fig. 15. Pressure vs distance from the taphole during the first instants after the impact.
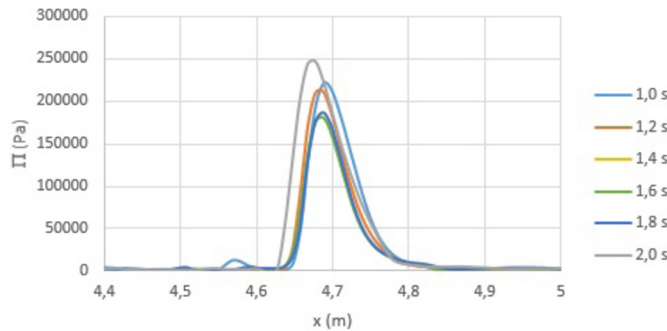
Fig. 16. Pressure vs distance from the taphole after 1.0 s of casting.

Table 11
Maximum values of pressure and corresponding point at different times.

t (s)	Π_{max} (Pa)	$x(\Pi_{max})$ (m)
1.0	221319	4.688
1.2	211837	4.688
1.4	217457	4.688
1.6	180123	4.688
1.8	186566	4.688
2.0	246389	4.678

6. Conclusions

A multiphase isothermal hydrodynamic model associated with turbulent flows of incompressible and immiscible fluids has been first described and then applied to a two-phase problem whose numerical simulation has been performed in a 2D computational domain. The interface dynamics was described by applying the Volume of Fluid (VOF) method, while the surface tension vector was provided by the Continuum Surface model (CSF). It allows to predict the hot metal jet evolution when running out of the blast furnace and the shear stress produced on the runner.

Due to the impossibility of making experimental measurements of shear stress on the runner, the tests of [1] for jets with normal impact have been considered as a reference and they have been numerically reproduced. The conclusion is that the SST $k - \omega$ turbulence model is the best choice for studying shear stress produced by a fluid jet on a wall.

Besides, relying on the works of [1] and [17], we have proposed an improvement of the classical equation to calculate the normalized shear stress by a jet impacting normally on a wall given by [1]. The validation of the proposed new formula has been carried out by comparing its resulting curve with the one obtained by numerically simulating each laboratory experiment using the SST $k - \omega$ turbulence model. The assessment of its adaptability to other scenarios has also been carried out by designing three additional numerical experiments with very good results.

Back to the 2D numerical simulation of the hot metal jet when running out of the blast furnace, a dynamic adaptive meshing technique is employed, following the progress of the jet with low computational costs. This has allowed to obtain the evolution of the shear stress on the impact zone of the runner. As it was expected, maximum shear stress occurs for the impact instant, and it decreases quickly. Two maxima with respect to the center of the jet and a minimum between them were located as well as their evolution with time. The maxima are not symmetric with respect to the center of the jet since its direction of impact is not normal to the runner. The impact point corresponds to the point with the maximum pressure and the minimum shear stress on the impact area.

The next step, once the mechanical impact stress has been computed, should be coupled it with the thermal one to compute thermomechanical shear stress, and then combine them with the eroded mass flux law to compute thermomechanical erosion (equations (1) or (2)).

References

[1] S. Beltaos, N. Rajaratnam, Impinging circular turbulent jets, J. Hydraul. Div. 100 (1974) 1313–1328.

[2] P. Barral, B. Nicolás, L.J. Pérez-Pérez, P. Quintela, Numerical simulation of wear-related problems in a blast furnace runner, in: Recent Advances in Differential Equations and Applications, in: SEMA SIMAI Springer Series, vol. 18, Springer, 2019, pp. 229–244.

[3] M. Geerdes, H. Toxopeus, C. van der Vliet, Modern Blast Furnace Ironmaking: An Introduction, IOS Press BV, 2009.

[4] S.J. Zhang, A.B. Yu, P. Zulli, B. Wright, P. Austin, Numerical simulation of solids flow in a blast furnace, Appl. Math. Model. 26 (2) (2002) 141–154, https://doi.org/10.1016/S0307-904X(01)00052-X.

[5] Y. Zhang, R. Deshpande, D.F. Huang, P. Chaubal, C.Q. Zhou, Numerical analysis of blast furnace hearth inner profile by using CFD and heat transfer model for different time periods, Int. J. Heat Mass Transf. 51 (1,2) (2008) 186–197, https://doi.org/10.1016/j.ijheatmasstransfer.2007.04.052.

[6] W.T. Cheng, E.N. Huang, S.W. Du, Numerical analysis on transient thermal flow of the blast furnace hearth in tapping process through CFD, Int. Commun. Heat Mass Transf. 57 (2014) 13–21, https://doi.org/10.1016/j.icheatmasstransfer.2014.07.007.

[7] S. Kuang, Z. Li, A. Yu, Review on modeling and simulation of blast furnace, Steel Res. Int. 89 (1) (2018) 1700071, https://doi.org/10.1002/srin.201700071.

[8] S. Vázquez-Fernández, A.G.-L. Pieiga, C. Lausín-Gónzalez, P. Quintela, Mathematical modelling and numerical simulation of the heat transfer in a trough of a blast furnace, Int. J. Therm. Sci. 137 (2019) 365–374, https://doi.org/10.1016/j.ijthermalsci.2018.11.025.

[9] P. Barral, B. Nicolás, P. Quintela, Numerical simulation of a jet impact during casting process in a blast furnace, in: Libro de Comunicaciones Definitivas Presentadas en CEDYA + CMA 2017, Cartagena, Spain, 2017, pp. 543–550.

[10] D.C. Wilcox, Turbulence Modelling for CFD, DCW Industries, LA, Cañada, California, 1998.

[11] R. Ariathurai, K. Arulanandan, Erosion rates of cohesive soils, J. Hydraul. Div. 104 (2) (1978) 279–283.

[12] F. Mercier, Numerical modelling of erosion of a cohesive soil by a turbulent flow, Ph.D. thesis, University of Aix-Marseille, 2013.

[13] F. Mercier, F. Golay, S. Bonelli, F. Anselment, R. Borghi, P. Phillipe, 2d axisymmetrical numerical modelling of the erosion of a cohesive soil by a sumerged turbulent impinging jet, Eur. J. Mech. B, Fluids 45 (2014) 36–50, https://doi.org/10.1016/j.euromechflu.2013.12.001.

[14] B. Nicolás, Simulación numérica de fenómenos de desgaste que afectan al canal principal del horno alto, Master's thesis, Industrial Mathematics, Universidade de Santiago de Compostela, 2017.

[15] G. Tryggvason, R. Scardovelli, S. Zaleski, Direct Numerical Simulations of Gas-Liquid Multiphase Flows, Cambridge University Press, 2011.

[16] S. Blairs, Sound velocity of liquid metals and metalloids at the melting temperature, Phys. Chem. Liq. 45 (4) (2007) 399–407, https://doi.org/10.1080/00319100701272084.

[17] P. Bradshaw, E.M. Love, The normal impingment of a circular air jet over a flat surface, Reports and Memoranda, Aeronautics Research Council, England 3205, 1961.

[18] D.J. Phares, G.T. Smedley, R.C. Flagan, The wall shear stress produced by the normal impingement of a jet on a flat surface, J. Fluid Mech. 418 (2000) 351–375, https://doi.org/10.1017/S002211200000121X.

[19] M. Mitchell, B. Muftakhidinov, T. Winchen, Engauge digitizer software, http://markummitchell.github.io/engauge-digitizer/, 2019.

[20] F.R. Menter, Two-equation eddy-viscosity turbulence models for engineering applications, AIAA J. 32 (1994) 1598–1605, https://doi.org/10.2514/3.12149.

[21] F. Bode, K. Sodjavi, A. Meslem, I. Nastase, Numerical prediction of wall shear rate in impinging cross-shaped jet at moderate Reynolds number, U.P.B. Sci. Bull., Series D: Mech. Eng. 76 (2014) 251–258.

[22] C.D. Argyropoulos, N.C. Markatos, Recent advances on the numerical modelling of turbulent flows, Appl. Math. Model. 39 (2) (2015) 693–732, https://doi.org/10.1016/j.apm.2014.07.001.

[23] A. Bermúdez de Castro, Continuum Thermomechanics, Progress in Mathematical Physics, Birkhäuser, Basel, 2005.

[24] D.A. Drew, S.L. Passman, Theory of Multicomponent Fluids, Applied Mathematical Sciences, vol. 135, Springer, New York, 1999.

[25] J.U. Brackbill, D.B. Kothe, C. Zemach, A continuum method for modeling surface tension, J. Comput. Phys. 100 (1992) 335–354, https://doi.org/10.1016/0021-9991(92)90240-Y.

[26] M. Wörner, W. Sabisch, G. Grötzbach, D.G. Cacuci, Volume-averaged conservation equations for volume-of-fluid interface tracking, in: Proceedings of the 4th International Conference on Multiphase Flow, New Orleans, Louisiana, USA, 2001.

[27] Fluent® 15.0 Theory Guidev, ANSYS edition, 2013.

[28] C.W. Hirt, B.D. Nichols, Volume of fluid (VOF) method for the dynamics of free boundaries, J. Comput. Phys. 39 (1981) 201–225, https://doi.org/10.1016/0021-9991(81)90145-5.